

1 **Optical and microphysical characterization of aerosol**
2 **layers over South Africa by means of multi-**
3 **wavelength depolarization and Raman lidar**
4 **measurements**

5

6 **E. Giannakaki^{1,a}, P.G. van Zyl², D. Müller³, D. Balis⁴ and M. Komppula¹**

7

8 (1){Finnish Meteorological Institute, P.O.Box 1627, FI-70211, Kuopio, Finland}

9 (2){Unit for Environmental Sciences and Management, North-West University,
10 Potchefstroom, South Africa}

11 (3){School of Physics, Astronomy and Mathematics, University of Hertfordshire,
12 Hatfield, United Kingdom}

13 (4){Laboratory of Atmospheric Physics, Thessaloniki, Greece}

14 ^a on leave from {Department of Environmental Physics and Meteorology, Faculty of
15 Physics, University of Athens, Athens, Greece}

16

17 Correspondence to: Elina Giannakaki (eleni.giannakaki@fmi.fi)

18

19 **Abstract**

20 Optical and microphysical properties of different aerosol types over South Africa
21 measured with a multi-wavelength polarization Raman lidar are presented. This study
22 could assist in bridging existing gaps relating to aerosol properties over South Africa,
23 since limited long-term data of this type is available for this region. The observations
24 were performed under the framework of the EUCAARI campaign in Elandsfontein.
25 The multi-wavelength Polly^{XT} Raman lidar system was used to determine vertical
26 profiles of the aerosol optical properties, i.e. extinction and backscatter coefficients,
27 Ångström exponents, lidar ratio and depolarization ratio. The mean microphysical
28 aerosol properties, i.e. effective radius and single scattering albedo were retrieved
29 with an advanced inversion algorithm. Clear differences were observed for the
30 intensive optical properties of atmospheric layers of biomass burning and
31 urban/industrial aerosols. Our results reveal a wide range of optical and microphysical
32 parameters for biomass burning aerosols. This indicates probable mixing of biomass
33 burning aerosols with desert dust particles, as well as the possible continuous
34 influence of urban/industrial aerosol load in the region. The lidar ratio at 355 nm, the
35 lidar ratio at 532 nm, the linear particle depolarization ratio at 355 nm and the
36 extinction-related Ångström exponent from 355 to 532 nm were 52 ± 7 sr; 41 ± 13 ;
37 0.9 ± 0.4 % and 2.3 ± 0.5 , respectively for urban / industrial aerosols, while these
38 values were 92 ± 10 sr; 75 ± 14 ; 3.2 ± 1.3 % and 1.7 ± 0.3 respectively for biomass
39 burning aerosols layers. Biomass burning particles are larger and slightly less
40 absorbing compared to urban / industrial aerosols. The particle effective radius were
41 found to be 0.10 ± 0.03 μm , 0.17 ± 0.04 μm and 0.13 ± 0.03 μm for urban/industrial,
42 biomass burning, and mixed aerosols, respectively, while the single scattering albedo
43 at 532 nm were 0.87 ± 0.06 , 0.90 ± 0.06 , and 0.88 ± 0.07 (at 532 nm), respectively for

44 these three types of aerosols. Our results were within the same range of previously
45 reported values.

46

47 **1. Introduction**

48 Atmospheric aerosols of natural and anthropogenic origin contribute substantially to
49 global climate variability (IPCC, 2013). Currently, the magnitude of the
50 (anthropogenic) aerosol impact on climate causes the largest uncertainty on our
51 knowledge of climate change (Forster et al., 2007). Large uncertainties exist due to
52 the diversity, not only with respect to aerosol particle size, composition, sources and
53 lifetime variation, but also with regard to the spatial and temporal distributions of
54 aerosols. Thus, the impacts of aerosols on climate must be understood and quantified
55 on a regional scale rather than on a global-average basis (Piketh et al., 2002).

56 High-quality aerosol measurements in the southern hemisphere are rather limited.
57 South Africa is located at the southernmost tip of the African continent, extending
58 from 22° S to 34° S latitude and from 16° E to 32° E longitude. Previous studies have
59 indicated that South Africa is one of the countries in the world that is largely affected
60 by aerosol load, due to various natural and anthropogenic sources (Piketh et al., 2000;
61 Piketh et al., 2002; Formenti et al., 2002, 2003; Campbell et al., 2003; Eck et al.,
62 2003; Freiman and Piketh, 2003; Ichoku et al., 2003; Ross et al., 2003; Winkler et al.,
63 2008; Queface et al., 2011; Tesfaye et al., 2011; Venter et al., 2012; Tiitta et al.,
64 2014). Intensive efforts have been undertaken during recent years to characterize
65 aerosol pollution in South Africa. In general, previous studies pointed at the
66 importance of regional circulation of air masses and seasonal pollutant variation. The
67 optical properties of aerosols have been studied by means of sun photometers (e.g.
68 Queface et al., 2011; Eck et al., 2003), *in situ* data (e.g. Laakso et al., 2012) and
69 satellite observations (e.g. Tesfaye et al., 2011) in these studies, which are based on
70 columnar aerosol optical properties. Ground-based Raman lidars provide vertically
71 resolved information on the distribution and optical properties of aerosols. Giannakaki

72 et al. (2015) used Raman lidar data obtained over a one year period at Elandsfontein
73 in South Africa ($26^{\circ}15' S$, $29^{\circ}26' E$, 1745 m above sea level (a.s.l.)) to study the
74 geometrical characteristics, intensive and extensive optical properties of free-
75 tropospheric aerosol layers. In addition to these characteristics that can be determined
76 with lidar data, multi-wavelength Raman lidar measurements can also be used to
77 determine profiles of microphysical particle properties by using inversion algorithms
78 (Twomey, 1977; Veselovskii et al., 2002, Müller et al., 2001). In this study we expand
79 our study of aerosols in South Africa by providing information on the microphysical
80 and optical properties of aerosol layers. This type of aerosol lidar observations are
81 valuable for spaceborne lidars such as CALIPSO (Cloud-Aerosol Lidar and Infrared
82 Pathfinder Satellite Observations) (e.g. Omar et al., 2009), since lidar ratio values for
83 different aerosol types are required for reliable aerosol extinction retrievals.
84 Therefore, this study could be useful for further improving lidar ratio selection-
85 scheme algorithms used in spaceborne lidar missions.

86 Four long-term ground-based aerosol measurements were carried out at sites in
87 economically growing countries in Asia, Africa and South America within the
88 EUCAARI project (Kulmala et al., 2011), which included Elandsfontein in South
89 Africa. The aim of EUCAARI was to characterize particles in terms of physical,
90 optical and chemical aerosol properties. Here we report lidar observations that were
91 performed at Elandsfontein. In particular, we discuss the optical and microphysical
92 properties of aerosol layers that are caused by biomass burning and urban/industrial
93 activities at the site. We present aerosol lidar ratios, particle linear depolarization
94 ratios and Ångström exponents for biomass burning and urban/industrial aerosol
95 layers measured with a multi-wavelength Raman lidar. The possible effect of desert
96 dust particles on biomass burning aerosol layers in terms of the intensive optical and

97 microphysical properties is also addressed. In addition, effective radius and single-
98 scattering albedo are calculated with an advanced inversion algorithm.

99 The paper is organized as follows: In section 2, the research site, the methodology
100 used for the retrieval of optical and microphysical properties and the aerosol typing
101 are introduced. As a case study, the arrival of a biomass burning aerosol layer over
102 Elandsfontein is discussed in section 3. Section 4 presents the main findings of the
103 optical and microphysical aerosol properties for selected biomass burning,
104 urban/industrial and mixed aerosol layers. We close our contribution with a summary
105 and conclusion in section 5.

106 **2. Location and Methodology**

107 **2.1. Measurement site**

108 The measurement site was located on a hill top at Elandsfontein ($26^{\circ}15' \text{ S}$, $29^{\circ}26' \text{ E}$,
109 1745 m a.s.l.) in the Highveld region of South Africa. The station was located
110 approximately 150 km east of the Johannesburg-Pretoria megacity, which is the
111 largest metropolitan area in South Africa with a population of more than 10 million
112 people (Lourens et al., 2012).

113 In South Africa, anthropogenic atmospheric emissions are predominantly the product
114 of industrial activities and biomass burning (Ross et al., 2003). South Africa is the
115 most industrialized country of the sub-continent – primarily due to the industrialized
116 Highveld region (Freiman, 2003; Wenig et al., 2003). This region has clusters of
117 industrial complexes and power plants between 25.5° S , 27.5° E and 27.0° S , 30.5° E
118 (Ross et al., 2003), which contributes significantly to aerosol and trace gases pollution
119 (Freiman et al., 2003). Tropospheric NO_2 distributions derived with SCIAMACHY
120 (SCanning Imaging Absorption spectroMeter for AtmosphericCHartography) from
121 August 2002 to March 2012 (Schneider et al., 2015) are presented in Figure 1. The
122 tropospheric NO_2 column density of the Highveld region in South Africa is

123 comparable to that observed over central and northern Europe, eastern North America
124 and Southeast Asia (Lourens et al, 2012).

125 In addition, emissions from biomass burning (wild fires) contribute significantly to
126 regional emission loads (e.g. Giannakaki et al., 2015). Both, natural phenomena
127 (lightning) and human induced activities are responsible for biomass burning
128 (Edwards et al., 2006). The number of hotspots, with confidence levels between 80-
129 100%, (<http://earthdata.nasa.gov/data/nrt-data/firms/active-fire-data>), in the latitude
130 range between -40° and 40° and longitude range between -20° and 60° are plotted in
131 Figure 2. The number of hotspots is averaged in terms of 3 months for the year 2010.
132 Wild fires originate in the sub-equatorial central African region and progress
133 southward (Roy et al., 2005). In southern Africa, the fires progress along a north-west
134 to south-east track.

135 **2.2. Description of the lidar system and lidar data processing**

136 The transportable aerosol Raman lidar Polly^{XT} that was operated remotely at
137 Elandsfontain is described by Althausen et al. (2009) and Engelmann et al. (2016).
138 Polly^{XT} works with a Nd:YAG laser emitting at its primary wavelength of 1064 nm,
139 which after frequency doubling and tripling emits at the wavelengths of 532 and 355
140 nm, respectively. The receiver consists of a Newtonian telescope with a diameter of
141 300 mm and a field of view of 1 mrad. Photomultiplier tubes (PMT) are used for the
142 detection of the elastically backscattered photons at 355, 532 and 1064 nm, as well as
143 the in-elastically backscattered photons at 387 and 607 nm that correspond to the
144 Raman-shift by nitrogen molecules at 355 and 532 nm, respectively. Additionally, the
145 cross-polarized component at 355 nm is detected and consequently allows for the
146 determination of the linear particle depolarization ratio (also called depolarization
147 ratio). To retrieve the particle depolarization ratio the Rayleigh calibration method
148 was applied within the data analysis under the assumption of pure Rayleigh

149 depolarization in an aerosol-free height range (Behrendt and Nakamura, 2002). The
150 vertical resolution of the signal profiles is 30 m and the raw data are typically stored
151 as 30 s average values (20 Hz laser frequency). Data were collected on the web page
152 of PollyNet (<http://polly.tropos.de>) where the “quicklooks” of all measurements are
153 available.

154 Extinction and backscatter coefficient profiles at 355 and 532 nm, respectively, were
155 obtained with the Raman method (Ansmann et al., 1992). To vertically retrieve the
156 backscatter coefficient at 1064 nm we use Fernald-Klett method (Fernald, 1984; Klett,
157 1981). With this method the particle backscatter coefficient is derived applying a
158 backward iteration starting at a chosen reference height. The method requires
159 independent information on the lidar ratio and on the reference value of the particle
160 backscatter coefficient. The cases analyzed here are night-time measurements and the
161 retrieved backscatter at 1064 nm was also evaluated by the Raman method (Ansmann
162 et al., 1992) using also the signal from the Nitrogen Raman channel at the 607 nm. An
163 overlap correction was applied on the basis of a simple technique proposed by
164 Wandinger and Ansmann (2002). The depolarization ratio, i.e. the ratio of the cross-
165 polarized to the parallel-polarized component of the backscatter coefficient (particles
166 and molecules) at 355 nm was also calculated. The contribution of the molecules can
167 easily be calculated, which then provides the linear particle depolarization ratio (Cairo
168 et al., 1999; Murayama et al., 1999).

169 The uncertainties affecting the retrieval of extinction and backscatter coefficients, and
170 thus the calculation of lidar ratio and Ångström exponents are mainly due: to the
171 statistical error due to signal detection, the systematic error associated with the
172 estimation of the atmospheric molecular number density from the pressure and
173 temperature profiles, the systematic error associated with the evaluation of the aerosol

174 scattering wavelength dependence, the systematic error for overlap function, the
175 errors introduced by operation procedure such as signal binning (smoothing) and
176 averaging accumulating lidar returns. The overall relative errors of the lidar-derived
177 aerosol properties range between 5%-15% for the backscatter coefficients, 10%-30%
178 for the extinction coefficients, 20%-40% for the Ångström exponents, 15%-40% for
179 the lidar ratios and approximately 5%-10% for the linear particle depolarization ratio
180 (Hänel et al., 2012; Baars et al., 2016, Engelmann et al., 2016). A detailed discussion
181 on the influence of aerosol optical depth errors to Ångström exponent errors can be
182 found in Wagner et al., 2008.

183 The layer identification was based on the assumption that the optical properties should
184 be relatively stable. This means that within a chosen height layer, the variability of the
185 optical data should be less than the statistical uncertainty of the individual data points.
186 In Table 1 we provide information regarding the elevated layers that were selected for
187 the optical and microphysical aerosol characterization. The characterization of aerosol
188 types will be discussed in section 2.4.

189

190 **2.3. Retrieval of microphysical properties**

191 Microphysical particle properties are derived with an inversion algorithm that has
192 been developed at the Leibniz Institute for Tropospheric Research. A detailed
193 description of the inversion code is given by Müller et al (1999a, 1999b). A minimum
194 of three backscatter coefficients (355, 532, and 1064 nm) and two extinction
195 coefficients (355 and 532 nm), with measurement errors less than 30%, are required
196 as input in order to obtain microphysical results that have reasonably low
197 uncertainties (Müller et al., 2001). The selection of the individual inversion solutions
198 is based on the concept that the back-calculated optical data should agree with the
199 original data within the limits of the measurement errors, and that a pre-selected

200 discrepancy level, which is an output parameter of the inversion algorithm (Müller et
201 al., 1999a), is not exceeded. The mean particle size in terms of the effective radius is
202 then calculated along with the standard deviation from these selected individual
203 solutions. One also obtains a range of complex refractive indexes by applying this
204 method. The complex refractive index is a wavelength-independent quantity.
205 Therefore, inversion can only provide a wavelength-independent value that represents
206 the entire range of wavelengths from 355 – 1064 nm. The single-scattering albedo can
207 then be calculated from the volume concentration distribution, which is another data
208 product of the inversion algorithm, and the associated mean complex refractive index
209 by means of a Mie scattering algorithm.

210 Uncertainties associated with the retrievals are in general <30% for effective radius.
211 The real part of the complex refractive index is derived to an accuracy better than
212 ± 0.1 , while the imaginary part is obtained for its correct order of magnitude if the
213 value is <0.01i (for larger values of the imaginary part the uncertainty is <50%). The
214 single-scattering albedo can be calculated with an accuracy of ± 0.05 , if uncertainties
215 of the input optical data are on average <10-15%. A detailed error analysis is
216 presented by Müller et al. (1999b, 2001) and Veselovskii et al., (2002, 2004).

217 **2.4. Aerosol classification**

218 The identification of the source of aerosol particles is possible with the synergetic use
219 of in-situ and satellite measurements, as well as utilizing model estimations.

220 The HYSPLIT_4 (Hybrid Single Particle Lagrangian Integrated Trajectory) model
221 (Draxler and Hess, 1997) was used to compute backward air mass trajectories
222 employing the kinematic approach and by using the re-analysed National Oceanic and
223 Atmospheric Administration (NOAA) dataset with a resolution of $2.5^\circ \times 2.5^\circ$ (latitude,
224 longitude) as input. Four-day backward trajectories were selected, because they
225 extend far enough back in time and distance to cover the main source regions

226 suspected to affect the region investigated. The trajectories were calculated for the
227 center of the layer observed and for the time of the lidar measurement.

228 The number of fire hotspots is given by Moderate Resolution Imaging
229 Spectroradiometer (MODIS) collection-5 active-fire product data (Giglio, L. et al.,
230 2010). The number of hotspots, obtained from MODIS for four days prior to each of
231 the measurements, was superimposed on the trajectory analysis map in order to detect
232 the presence of smoke particles over our site for the cases analyzed.

233 Trace gases were measured as part of routine air quality monitoring at the site by the
234 national electricity supplier, i.e. Eskom. A Thermo Electron 43C SO₂ analyser and a
235 Thermo Electron 42i NO_x analyser were used to measure SO₂ and NO_x respectively.
236 H₂S was measured with a Thermo Electron 43A SO₂ analyzer with a Thermo Electron
237 340 converter. 15-minute data were averaged for the extent of measurement time for
238 each of the measurements periods (Table 1). For instances where the combined use of
239 trajectory analysis and fire hotspots did not indicate the presence of biomass burning
240 aerosols we checked whether the measured NO_x, SO₂ or H₂S concentrations were
241 higher than the seasonal mean values of that measured for the entire period of the
242 EUCAARI campaign. These seasonal mean values are presented in Laakso et al.
243 (2012). In addition, when the trace gases concentrations were lower than the mean
244 seasonal values measured during the EUCAARI campaign and biomass-burning
245 activity or desert dust advection were absent, we checked if the daily concentration of
246 the trace gases exceeded the mean critical values.

247 There were also cases that indicated desert dust aerosol particles in addition to the
248 smoke, which originated either from the Kalahari or the Namibia desert that could
249 have additionally contributed to the aerosol loads. Therefore, the measured aerosol
250 optical properties determined for these cases were attributed to a mixing state where

251 smoke particles were possible to be mixed with desert dust aerosols. Additional
252 mixing with urban / industrial aerosols is also possible.

253 An example of a measurement of biomass burning aerosols is discussed in the
254 subsequent section in order to demonstrate the methodology used to derive the optical
255 and microphysical aerosol properties.

256
257 **3. Biomass burning aerosols on 1st October 2010 at Elandsfontein,**
258 **South Africa**

259 In this section we will study a geometrically deep layer that extends up to 2.1 km
260 height above ground level (AGL) as observed on the 1st of October 2010. The
261 atmospheric structure, in terms of range corrected signals, is quite stable which
262 indicates similar optical properties throughout the layer
263 (<http://polly.tropos.de/?p=bilder&lambda=1064&Jahr=2010&Monat=10&Tag=1&Ort=11#bildanker>). High backscatter returns are observed on the day when the
265 measurement is conducted in relation to the previous and the next day (as can be
266 already seen in Figure 4 (a) – light green).

267 MODIS fire hotspots product reveal that several fires were active during the period
268 28th of September 2010 – 1st of October 2010 as shown in Figure 3 (a). In Figure 3
269 (b), four-day backward trajectories arriving at Elandsfontein on 1st of October 2010 at
270 00:00 are presented. The trajectories are computed for arrival heights of the bottom,
271 center and top of the observed layer. The trajectory analysis along with MODIS fire
272 hotspots reveals that the air masses are highly possible to carry smoke particles at
273 Elandsfontein on the day of the measurement.

274 In Figure 4 the optical lidar profiles are presented. The backscatter and extinction
275 maximum at all three wavelengths were observed within the 0.9 to 1.9 km height
276 range. High values of the lidar ratio of 96 ± 5 sr at 355 nm and 89 ± 5 sr at 532 nm

277 indicate that the smoke particles inside this layer were most likely highly light-
278 absorbing . The Ångström exponent, related to extinction between 355 and 532 nm,
279 was 1.8 ± 0.1 , which points to comparably small particles and indicative of fresh
280 smoke (eg. Müller et al., 2005). A constant particle depolarization ratio in the order
281 of 4% is observed at 355 nm throughout the layer. The lack of significant vertical
282 variability of the lidar ratio, the Ångström exponent and the particle depolarization
283 ratio suggests the presence of the same type (biomass burning) of aerosols throughout
284 the layer.

285 The mean values of extinction (at 355 and 532 nm) and backscatter coefficients (at
286 355, 532 and 1064 nm) were calculated within the defined layer and were used as
287 input in the inversion algorithm. Effective radius, complex refractive index and
288 single-scattering albedo were calculated with the microphysical inversion code. An
289 effective radius of $0.15 \pm 0.02 \mu\text{m}$ was determined, while the single-scattering albedo
290 was approximately 0.86 at 532 nm that indicates relatively strong-absorbing aerosols.

291 **4. Results and Discussion**

292 We performed optical lidar data analysis, microphysical retrievals and aerosol typing
293 for each of the thirty eight aerosol layers listed in Table 1 in the same way as
294 presented in the example in section 3. Each aerosol layer in Table 1 was classified
295 into one of the three aerosol types, i.e. urban/industrial, biomass burning, and mixed
296 aerosols after thorough visual inspection of the backward trajectories, MODIS
297 hotspots fires products and in-situ aerosol observations, as explained in section 2.4.
298 Table 2 summarizes the mean intensive optical properties (lidar ratio at 355 and 532
299 nm, depolarization ratio at 355 nm and Ångström exponent related to extinction
300 between 355 and 532 nm) presented together with the associated standard deviations,
301 ranges (minimum and maximum values) and medians.

302 Figure 5 presents the particle lidar ratios at 355 nm versus the extinction-related
303 Ångström exponent for urban/industrial (black), biomass burning (red) aerosol layers
304 as well as for the mixed aerosol layers (green). Different aerosol types occupy
305 different areas in the Ångström-exponent–lidar-ratio plot. Aerosols from urban and
306 industrial activities are on average characterized by larger Ångström exponents than
307 (pure or mixed) biomass burning aerosols. The lidar ratios of biomass burning
308 aerosols are among the highest compared to literature with a mean value of 92 ± 10 sr
309 (e.g. Müller et al., 2007; Nicolae et al, 2013; Amiridis et al., 2009). Urban / Industrial
310 aerosol layers were found to have lower lidar ratio values in the range between 41 and
311 59 sr at 355 nm. Our results indicate that biomass burning aerosols have lower lidar
312 ratios when they are mixed either with desert dust aerosols or with urban / industrial
313 aerosols. This might be due to the non-spherical shape of desert dust that may have a
314 significant effect on the lidar ratio. Model calculations show that a deviation from the
315 spherical shape can efficiently increase particle backscattering and thus lower the lidar
316 ratio (Mishchenko et al., 1997), which was also confirmed by Müller et al. (2003).
317 Ångström exponent values of these aerosols ranged from 1.6 to 2.5, with a mean value
318 of 2.0 ± 0.4 , which is larger (smaller particles) than the mean value of 1.7 ± 0.3 we
319 observed for ‘pure’ biomass burning aerosols. The role that hot air close to the surface
320 of the earth plays in generating these dust size distribution is not well understood
321 (Nisantzi et al., 2014). Wind stress close to the surface may be very complex and the
322 sudden release of all the moisture in the hot soil particles may strongly influence the
323 cracking of larger particles into smaller ones and thus lead to a much more
324 complicated size distribution than observed during desert dust outbreaks (Mamouri et
325 al., 2014).

326 It is evident from Figure 5 that Ångström exponent values for the different aerosol
327 types overlap. Therefore, another intensive aerosol property, the linear particle
328 depolarization ratio, which is an indicator of non-spherical particles, was also used.
329 Figure 6 shows the lidar ratio at 355 nm versus the depolarization ratio at the same
330 wavelength for the three aerosol types. Different clusters of data pairs can be
331 identified. Lower depolarization ratio values were found for urban/industrial aerosol
332 layers. These aerosol layers are also characterized by lower lidar ratios and thus the
333 data points representing urban / industrial pollution occupy the lower left region in
334 Figure 5. Significantly larger particle linear depolarization ratios with a mean of $8.3 \pm$
335 0.7% were found for mixed aerosols. Typical desert dust aerosol depolarization ratios
336 determined in field measurements performed in the northwestern corner of the Sahara
337 ranged from 30 to 35% at 532 nm with a mean value of $31 \pm 3\%$ (Freudenthaler et al.,
338 2009). In addition, particle depolarization ratios ranging between 30 to 35% were also
339 observed for Asian desert dust (Sugimoto et al., 2003, Shimizu et al., 2004, Shin et
340 al., 2015) and desert dust originating from Middle East dust sources (Mamouri et al.,
341 2013). Depolarization ratios of the mixtures of biomass burning aerosols and desert
342 dust particles determined for African biomass burning and dust mixtures ranged
343 between 8 – 26% at 532 nm (Weinzierl et al., 2011, Tesche et al., 2009). Therefore
344 depolarization values reported in this study are at the lower end of these values. This
345 observed difference can be attributed to the different contribution of desert dust
346 particles to the biomass burning plume. However, we should also note that the
347 geometrical shape of the dust particles over the Kalahari desert could be different
348 from the shape of Saharan dust. Also, the possible influence of the background urban
349 / industrial aerosols in the mixture should be kept in mind.

350 A wide range of (lower) depolarization ratios and lidar ratios was found for biomass
351 burning aerosols. This observed variability can be attributed to differences in the
352 chemical composition of the particles that depends on the source region, relative
353 humidity in the atmosphere, the type of fire, or the combined effect of these factors. In
354 addition, the mixing of the biomass burning aerosols with maritime or even
355 urban/industrial background aerosols cannot be excluded as a possible reason for the
356 variability of lidar ratio and depolarization ratio values.

357 Several statistics of lidar ratios and Ångström exponents for different aerosol types in
358 the world are available for comparison. Figure 7 provides some of the general
359 literature with regard to the lidar ratios values at 355 nm and Ångström exponents of
360 urban/industrial and biomass-burning aerosols, as well as for mixtures of biomass
361 burning and desert dust aerosols. To interpret the x-axis of the Figure 7 one should
362 also look the Table 4. It is evident from Figure 7 that intensive aerosol properties are
363 in good agreement with values found from other studies.

364 The lidar ratio at 355 nm, in particular, shows similar values for urban / industrial
365 aerosols in various regions of the world. Ångström exponent values found for
366 urban/industrial particles in this study are at the upper limit of results previously
367 published for this aerosol type, which indicates slightly smaller particles at
368 Elandsfontein that can most probably be ascribed by differences in the emission
369 sources. The depolarization ratio is at the lower limit indicating spherically shaped
370 anthropogenic particles.

371 The lidar ratio for biomass burning aerosol layers is within the range of previously
372 reported values, although the values tend to be more at the upper limit of the reported
373 values. The Ångström exponents are in very good agreement with previous studies.
374 Müller et al. (2007) studied the growth of free-tropospheric forest fire smoke particles

375 and indicated that the Ångström exponent decreases with the duration of transport.
376 The Ångström exponent values found in this study (1.7 ± 0.3) corresponds to travel
377 times of the biomass burning aerosols between 1 and 3 days, which is confirmed by
378 back-ward trajectory analysis. The characteristics of biomass burning emissions in the
379 subtropical South African region vary according to the type of fuel burned (vegetation
380 type), meteorology and combustion phase (Ross et al., 2003). For example, flaming
381 grass fires produce smoke with more soot compared to smoke emitted from
382 smoldering wood and bush fires (Posfai et al., 2003). Thus differences in the chemical
383 composition of the particles might be one of the reasons for the observed large lidar
384 ratio.

385 For the mixed aerosols the lidar ratio values reported here are in very good agreement
386 with previous studies for the mixture of desert dust and biomass burning aerosols. The
387 contribution of desert dust particles within the observed biomass burning plumes is
388 probably lower, thus resulting in a lower depolarization ratio and larger Ångström
389 exponent than what has been reported in literature for biomass burning mixed with
390 dust as mentioned previously. Groß et al. (2011) reported neutral wavelength-
391 dependence of the particle depolarization ratios for mixed dust and smoke layers for
392 which Ångström exponents varied between 0.12 and 0.16, while Tesche et al. (2011)
393 reported wavelength-independent linear particle depolarization ratios of 0.12-0.18 at
394 355, 532 and 710 nm for mixed dust and smoke layers. In that sense our results on
395 particle depolarization ratios at 355 nm are similar to results from these studies
396 reporting linear particle depolarization ratio at 532 nm.

397 In Figure 9 the effective radius against the Ångström exponent is plotted. In general
398 the plot shows the same features already noted for Figure 5. On average the largest
399 aerosols are determined for biomass burning aerosols (red) with an effective radius of

400 $0.17 \pm 0.04 \mu\text{m}$. Particles from anthropogenic pollution (black) are smaller with a
401 mean effective radius of $0.1 \pm 0.03 \mu\text{m}$. Our results indicate that the influence of
402 Kalahari desert dust on biomass burning plumes leads to smaller particles compared
403 to pure biomass burning aerosols with a mean effective radius of $0.13 \pm 0.03 \mu\text{m}$.
404 Mean microphysical properties i.e. effective radius, single scattering albedo and
405 complex refractive index are listed with their associated standard deviations, ranges
406 (minimum and maximum values) and medians in Table 3. The particles in the
407 biomass-burning aerosol layers show a mean effective radius of $0.17 \pm 0.04 \mu\text{m}$,
408 which is within the range of values reported in previous studies for biomass burning
409 aerosols. Reid et al. (1998) reported count median diameter values ranging from 0.12
410 μm for fresh particles to $0.21 \mu\text{m}$ for aged particles near rain-forest fires in Brazil.
411 Radke et al. (1988) obtain values of approximately $0.22 \mu\text{m}$ for particles from forest
412 fires in North America. Wandinger et al. (2002) found larger biomass burning
413 aerosols with an effective radius of approximately $0.25 \mu\text{m}$. Effective radii in the
414 range between 0.19 and $0.44 \mu\text{m}$ were found for biomass burning aerosol layers
415 resulting from long-range transport across Romania (Nicolae et al., 2013). Müller et
416 al, (2007) presented values ranging between 0.13 and $0.15 \mu\text{m}$ for plumes ageing
417 between one to three days.
418 The three types of aerosols cover a wide range of single-scattering albedo values as
419 shown in Table 3. The mean single-scattering albedo for biomass burning aerosol is
420 0.90 ± 0.06 (at 532 nm). Lower single scattering albedos are reported in literature for
421 fresh biomass burning particles in Europe. Nicolae et al. (2013) reported a value of
422 0.78 ± 0.02 , while Reid et al. (1998) found that single scattering albedo ranges
423 between 0.74 and 0.77 for fresh smoke. Previous studies show that aged biomass
424 burning layers are characterized by larger single scattering albedos. For example,

425 Murayama et al. (2004) found a value of 0.95 ± 0.06 at 532 nm, while Noh et al.
426 (2009) reported single scattering albedos of 0.92 at the same wavelength. Therefore
427 our results indicate moderately absorbing particles resulting from fresh or medium
428 aged (less than 3 days) biomass burning aerosols.

429 For the mixed aerosols we determined lower mean scattering-albedos of 0.88 ± 0.07 ,
430 which is slightly higher than the mean single-scattering albedo of 0.87 ± 0.06
431 determined for urban/industrial aerosol layers. Laakso et al. (2012) reported values of
432 0.84 ± 0.08 (637 nm) at ground level at Elandsfontein, South Africa. Quaface et al.
433 (2011) determined significantly larger values of 0.91 and 0.89 at 440 nm and 670 nm,
434 respectively, from AERONET data collected at Skukuza in South Africa. Our results
435 indicate that elevated anthropogenic aerosol layers from urban and industrial activities
436 are characterized by stronger light-absorption.

437 Complex refractive indexes are also reported in Table 3. Real parts of the complex
438 refractive index of these particles are mostly > 1.5 , while imaginary parts vary from
439 $0.007i$ to $0.04i$. Lower real parts of the refractive index are found for biomass burning
440 aerosols compared to the urban/industrial particulates with values ranging from 1.35
441 to 1.57. The imaginary parts of the refractive index of biomass burning aerosol layers
442 are $< 0.03i$ (with the exception of one case that shows an imaginary refractive index
443 of $0.046i$). A large variation of refractive indices for the real and imaginary parts is
444 observed for mixed aerosols. This might allude to the different levels of contribution
445 of Kalahari desert dust to biomass burning aerosol layers.

446

447 **5. Summary and Conclusions**

448 Thirty eight aerosol layers of urban/industrial, biomass burning, and mixed aerosols
449 were studied with regard to their optical and microphysical properties at

450 Elandsfontein, South Africa. The combination of Raman lidar observations with
451 backward trajectory analysis, satellite fire observations and *in situ* data allowed for
452 source identification of the elevated aerosol layers. Measurements of the lidar ratios
453 and depolarization ratios are presented in order to assist in the separation of
454 anthropogenic, biomass burning, and mixtures of aerosols.

455 A wide range of optical (lidar ratio and depolarization ratio) and microphysical (single
456 scattering albedo, complex refractive index) properties was determined for biomass
457 burning aerosols, indicating differences in chemical composition. Aerosols from
458 urban and industrial activities are on average characterized by larger Ångström
459 exponents than (pure or mixed) biomass burning aerosols. Lidar ratios for biomass
460 burning aerosols are among the highest found in literature with a mean value of $92 \pm$
461 10 sr, while the anthropogenic aerosols are characterized by lower lidar ratios in the
462 range between 41 and 59 sr at 355 nm. Ångström exponents were found to be similar
463 for all types of aerosol types under study, with slightly larger values determined for
464 anthropogenic aerosols. Mean effective radii of 0.17 ± 0.04 μm and 0.1 ± 0.03 μm
465 were calculated for biomass burning and urban / industrial aerosols, respectively. We
466 have also shown that in certain instances biomass burning aerosols may contain a
467 small amount of desert dust particles resulting in higher depolarization ratios and
468 lower lidar ratios than the values reported for pure biomass burning aerosols.
469 Moderately absorbing particles were found for biomass burning layers with a mean
470 single scattering albedo of 0.9 ± 0.06 . Mixed aerosols were found more absorbing
471 with a mean single-scattering albedo of 0.88 ± 0.07 . A slightly lower mean single-
472 scattering albedo of 0.87 ± 0.06 was found for urban / industrial aerosol layers.
473 However, this value was larger than the values reported for the same site from

474 ground-based in-situ measurements. Our optical and microphysical results for the
475 analyzed aerosol types agreed very well with similar studies reported in literature.
476 Ground-based lidar networks provide information on the vertical and horizontal
477 distribution of optical aerosol properties in a systematic and statistically significant
478 manner. Different lidar networks that are globally distributed observe aerosols in
479 Europe, South America, Asia and North America. The analysis of lidar measurements
480 presented here could assist in bridging existing gaps with regard to our knowledge of
481 the vertical distribution of optical and microphysical aerosols in the South African
482 atmosphere, since limited long-term data of this nature is available for this region. Our
483 results could also be useful for lidar ratio selection schemes needed for elastic-
484 backscatter lidars. In that sense our findings could be used in advancing lidar
485 algorithms used for present and/or future satellite lidar missions.

486

487

488 **ACKNOWLEDGMENTS**

489 This work has been partly supported by the European Commission 6th Framework
490 program under the EUCAARI project (contract no. 036833-2). Elina Giannakaki
491 acknowledges the support of the Academy of Finland (project no. 270108). The
492 authors acknowledge the staff of the North-West University for valuable assistance
493 and routine maintenance of the lidar. We also acknowledge Eskom and Sasol for their
494 logistical support for measurements at Elandsfontein.

495

496 **REFERENCES**

497 Alados Arboledas, L., Müller, D., Guerrero Rascado, J. L., Navas Guzmán, F., Pérez
498 Ramírez, D., and Olmo, F. J.: Optical and microphysical properties of fresh biomass
499 burning aerosol retrieved by Raman lidar, and star and sun-photometry, *Geophys.*
500 *Res. Lett.*, 38, L01807, doi:10.1029/2010GL045999, 2011.

501 Althausen, D., Engelmann, R., Baars, H., Heese, B., Ansmann, A., Müller, D., and
502 Komppula, M.: Portable Raman Lidar Polly^{XT} for Automated Profiling of Aerosol
503 Backscatter, Extinction, and Depolarization, *J. Atmos. Ocean. Technol.*, 26, 2366-
504 2378, doi: 10.1175/2009jtecha1304.1, 2009.

505 Amiridis, V., Balis, D. S., Giannakaki, E., Stohl, A., Kazadzis, S., Koukouli, M. E.,
506 and Zanis, P.: Optical characteristics of biomass burning aerosols over Southeastern
507 Europe determined from UV-Raman lidar measurements, *Atmos. Chem. Phys.*, 9,
508 2431-2440, doi:10.5194/acp-9-2431-2009, 2009.

509 Ansmann, A., Wandinger, U., Riebesell, M., Weitkamp, C., and Michaelis, W.:
510 Independent measurement of extinction and backscatter profiles in cirrus clouds by
511 using a combined Raman elastic-backscatter lidar, *Appl. Optics*, 31, 7113-7131, doi:
512 10.1364/AO.31.007113,1992.

513 Ansmann, A., Engelmann, R., Althausen, D., Wandinger, U., hu, M., Zhang, Y., and
514 He, Q.: High aerosol load over the Pearl River Delta, China, observed with Raman
515 lidar and Sun photometer, *Geophys. Res. Lett.*, 32, L13815, doi:
516 10.1029/2005GL023094, 2005.

517 Ansmann A., Baars, H., Tesche, M., Müller, D., Althausen, D., Engelmann, R.,
518 Pauliquevis, T., and Artaxo, P.: Dust and smoke transport from Africa to South
519 America : Lidar profiling over Cape Verde and the Amazon rainforest, *Geophys. Res.*
520 *Lett.*, 36, L11802, doi:10.1029/2009GL037923, 2009.

521 Baars, H., Ansmann, A., Althausen, D., Engelmann, R., Artaxo, P., Pauliquevis, T.,
522 and Souza, R.: Further evidence for significant smoke transport from Africa to
523 Amazonia, *Geophys. Res. Lett.*, 38, L20 802, doi: 10.1029/2011GL049200, 2011.

524 Baars, H., Ansmann, A., Althausen, D., Engelmann, R., Heese, B., Müller, D., Artaxo,
525 P., Paixao, M., Pauliquevis, T., and Souza, R.: Aerosol profiling with lidar in Amazon
526 Basin during the wet and dry season, *J. Geophys. Res.*, 117, D21201, doi:
527 10.1029/2012JD018338, 2012.

528 Baars, H., Kanitz, T., Engelmann, R., Althausen, D., Heese, B., Komppula, M.,
529 Preißler, J., Tesche, M., Ansmann, A., Wandinger, U., Lim, J.-H., Ahn, J. Y.,
530 Stachlewska, I. S., Amiridis, V., Marinou, E., Seifert, P., Hofer, J., Skupin, A.,
531 Schneider, F., Bohlmann, S., Foth, A., Bley, S., Pfüller, A., Giannakaki, E.,
532 Lihavainen, H., Viisanen, Y., Hooda, R. K., Pereira, S. N., Bortoli, D., Wagner, F.,
533 Mattis, I., Janicka, L., Markowicz, K. M., Achtert, P., Artaxo, P., Pauliquevis, T.,
534 Souza, R. A. F., Sharma, V. P., van Zyl, P. G., Beukes, J. P., Sun, J., Rohwer, E. G.,
535 Deng, R., Mamouri, R.-E., and Zamorano, F.: An overview of the first decade of
536 PollyNET: an emerging network of automated Raman-polarization lidars for
537 continuous aerosol profiling, *Atmos. Chem. Phys.*, 16, 5111-5137, doi:10.5194/acp-
538 16-5111-2016, 2016.

539 Balis, D.S., Amiridis, V., Zerefos, C., Gerasopoulos, E., Andreae, M., Zanis, P.,
540 Kazantzidis, A., Kazadzis, S. and Papayannis A.: Raman lidar and Sun photometric
541 measurements of aerosol optical properties over Thessaloniki, Greece during a
542 biomass burning episode 2003, *Atmos. Environ.*, 37(32), 4529–4538,
543 doi:10.1016/S1352-2310(03)00581-8, 2003.

544 Burton, S.P., Ferrare, R.A., Hostetler, C.A., Hair, J.W., Rogers, R.R, Obland, M.D.,
545 Butler, C.F., Cook, A.I., Harper, D.B., and Froyd, K.D.: Aerosol classification using
546 airborne High Spectral Resolution Lidar measurements – methodology and examples,
547 *Atmos. Meas. Tech.*, 5, 73-98, doi: 10.5194/amt-5-73-2012, 2012.

548 Burton, S.P., Ferrare, R.A., Vaughan, M.A., Omar, A.H., Rogers, R.R., Hostetler,
549 C.A., and Hair, J.W.: Aerosol classification from airborne HSRL and comparisons
550 with the CALIPSO vertical feature mask, *Atmos. Meas. Tech.*, 6, 1397-1412,
551 doi:10.5194/amt-6-1397-2013, 2013.

552 Cairo, F., Di Donfrancesco, G., Adriani, A., Pulvirenti, L. and Fierli, F.: Comparison
553 of various linear depolarization parameters measured by lidar, *Appl. Opt.* 38, 4425-
554 4432, doi: 10.1364/AO.38.004425,1999.

555 Campbell, J. R., Welton, E. J., Spinhirne, J. D., Ji, Q., Tsay, S. C., Piketh, S. J.,
556 Barenbrug, M., and Holben, B. N.: Micropulse lidar observations of tropospheric
557 aerosols over northeastern South Africa during the ARREX and SAFARI 2000 dry
558 season experiments, *J. Geophys. Res.*, 108, D13, 8497, doi: 10.1029/2002jd002563,
559 2003.

560 Draxler, R. R. and Hess, G. D.: Description of the HYSPLIT 4 modeling system,
561 NOAA Tech Memo, ERL ARL-224, 24, NOAA, Silver Spring, Md., 1997.

562 Eck, T. F., Holben, B. N., Ward, D. E., Mukelabai, M. M., Dubovik, O., Smirnov, A.,
563 Schafer, J. S., Hsu, N. C., Piketh, S. J., Queface, A., Le Roux, J., Swap, R. J., and
564 Slutsker, I.: Variability of biomass burning aerosol optical characteristics in southern
565 Africa during the SAFARI 2000 dry season campaign and a comparison of single
566 scattering albedo estimates from radiometric measurements, *J. Geophys. Res.*, 108,
567 D13, 8477, doi: 10.1029/2002jd002321, 2003.

568 Edwards, D.P., Emmons, L.K., Gille, J.C., Chu, A., Attie, Giglio, L., Wood, S.W.,
569 Haywood, J., Deeter, M.N., Massie, S.T., Ziskin, D.C., and Drummond, J.R.:
570 Satellite-observed pollution from Southern Hemisphere biomass burning, *J. Geophys.*
571 *Res.*, 111, doi: 10.1029/2005JD006655, 2006.

572 Engelmann, R., Kanitz, T., Baars, H., Heese, B., Althausen, D., Skupin, A.,
573 Wandinger, U., Komppula, M., Stachlewska, I. S., Amiridis, V., Marinou, E., Mattis,
574 I., Linné, H., and Ansmann, A.: The automated multiwavelength Raman polarization
575 and water-vapor lidar PollyXT: the neXT generation, *Atmos. Meas. Tech.*, 9, 1767–
576 1784, doi:10.5194/amt-9-1767-2016, 2016.

577 Formenti, P., Elbert, W., Maenhaut, W., Haywood, J., Osborne, S., and Andreae, M.
578 O.: Inorganic and carbonaceous aerosols during the Southern African Regional
579 Science Initiative (SAFARI 2000) experiment: Chemical characteristics, physical
580 properties, and emission data for smoke from African biomass burning, *J. Geophys.*
581 *Res.*, 108, D13, 16, doi: 10.1029/2002jd002408, 2003.

582 Formenti, P., Winkler, H., Fourie, P., Piketh, S., Makgopa, B., Helas, G., and
583 Andreae, M. O.: Aerosol optical depth over a remote semi-arid region of South Africa

584 from spectral measurements of the daytime solar extinction and the nighttime stellar
585 extinction, *Atmos. Res.*, 62, 11-32, doi: 10.1016/s0169-8095(02)00021-2, 2002.

586 Forster, P., Ramaswamy, V., Artaxo, P., Bernsten, T., Betts, R., Fahey, D., Haywood,
587 J., Lean, J., Lowe, D., Myhre, G., Nganga, J., Prinn, R., Raga, G., Schulz, M. and
588 Dorland, R. V.: Changes in atmospheric constituents and in radiative forcing. *Climate*
589 *Change 2007: The Physical Science Basis. Contribution of Working Group I to the*
590 *Fourth Assessment Report of the Intergovernmental Panel on Climate Change,*
591 *Cambridge Univ. Press, Cambridge, UK and New York, NY, USA, 129–234, 2007.*

592 Freiman, M. T., and Piketh, S. J.: Air transport into and out of the industrial Highveld
593 region of South Africa, *J. Appl. Meteorol.*, 42, doi: 10.1175/1520-
594 0450(2003)042<0994:ATIAOO>2.0.CO;2, 994-1002, 2003.

595 Freudenthaler, V., Esselborn, M., Wiegner, M., Heese, B., Tesche, M., Ansmann, A.,
596 Müller, D., Althausen, D., Wirth, M., Fix, A., Ehret, G., Knippertz, P., Toledano, C.,
597 Gasteiger, J., Garhammer, M., and Seefeldner, M.: Depolarization ratio pro- filing at
598 several wavelengths in pure Saharan dust during SAMUM 2006, *Tellus B*, 61, 165–
599 179, doi:10.1111/j.1600- 0889.2008.00396.x, 2009.

600 Giannakaki, E., Balis, D. S., Amiridis, V., and Zerefos, C.: Optical properties of
601 different aerosol types: seven years of combined Raman-elastic backscatter lidar
602 measurements in Thessaloniki, Greece, *Atmos. Meas. Tech.*, 3, 569-578, doi:
603 10.5194/amt-3-569-2010, 2010.

604 Giannakaki, E., Pfüller, A., Korhonen, K., Mielonen, T., Laakso, L., Vakkari, V.,
605 Baars, H., Engelmann, R., Beukes, J.P., Van Zyl, P.G., Josipovic, M., Tiitta, P.,
606 Chiloane, K., Piketh, S., Lihavainen, H., Lehtinen, K.E.J., and Komppula, M.: One
607 year of Raman lidar observations of free-tropospheric aerosol layers over South
608 Africa, *Atmos. Chem. Phys.*, 15, 5429-5442, doi: 10.5194/acp-15-5429-2015, 2015.

609 Giglio, L., Randerson, J. T., van der Werf, G.R., Kasibhatla, P. S., Collatz, G. J.,
610 Morton, D. C., and DeFries, R. S.: Assessing variability and long-term trends in
611 burned area by merging multiple satellite fire products, *Biogeosciences*, 7, 1171-1186,
612 doi: 10.5194/bg-7-1171-2010, 2010.

613 Groß, S., Esselborn, M., Weinzierl, B., Wirth, M., Fix, A., and Petzold, A.: Aerosol
614 classification by airborne high spectral resolution lidar observations, *Atmos. Chem.*
615 *Phys.*, 13, 2487-2505, doi: 10.5194/acp-13-2487-2013, 2013.

616 Groß, S., Tesche, M., Freudenthaler, V., Toledano, C., Wiegner, M., Ansmann, A.,
617 Althausen, D., and Seefeldner, M.: Characterization of Saharan dust, marine aerosols
618 and mixtures of biomass-burning aerosols and dust by means of multi-wavelength
619 depolarization and Raman lidar measurements during SAMUM 2, *Tellus B*, 63,706-
620 724, doi: 10.1111/j.1600-08892011.00556.x, 2011.

621 Hänel, A., Baars, H., Althausen, D., Ansmann, A., Engelmann, R., and Sun, Y. J.:
622 One-year aerosol profiling with EUCAARI Raman lidar at Shangdianzi GAW station:
623 Beijing plume and seasonal variation, *J. Geophys. Res.*, 117, D13201,
624 doi:10.1029/2012JD017577, 2012.

625 Heese, B., Althausen, D., Baars, H., Bohlmann, S., and Deng, R.: Aerosol properties
626 over Southeastern China from multiwavelength Raman and depolarization lidar
627 measurements, in: *Reviewed and Revised Papers of 27th ILRC International Laser Radar*
628 *Conference*, 5–10 July 10 2015, New York, USA, 2015.

629 Ichoku, C., Remer, L. A., Kaufman, Y. J., Levy, R., Chu, D. A., Tanre, D., and
630 Holben, B. N.: MODIS observation of aerosols and estimation of aerosol radiative
631 forcing over southern Africa during SAFARI 2000, *J. Geophys. Res.*, 108, 13, doi:
632 10.1029/2002jd002366, 2003.

633 Illingworth, A.J., Barker, H.W., Beljaars, A., Ceccaldi, M., Chepfer, H., Cole, J.,
634 Delanoë, J., Domenech, C., Donovan, D.,P., Fukuda, S., Hiraakata, M., Hogan, R.J.,
635 Huenerbein, A., Kollias, P., Kubota, T., Nakajima, T., Nakajima, T.Y., Nishizawa, T.,
636 Ohno, Y., Okamoto, H., Oki, R., Sato, K., Satoh, M., Shephard, M., Wandinger, U.,
637 Wehr, T., and Van Zadelhoff, G.-J.: THE EARTHCARE SATELLITE: The next step
638 forward in global measurements of clouds, aerosols, precipitation and radiation,
639 *Bulletin of the American Meteorological Society (BAMS)*,
640 doi: <http://dx.doi.org/10.1175/BAMS-D-12-00227.1>, 2015.

641 IPCC: The Physical Science Basis, Contribution of Working Group I to the Fifth
642 Assessment Report of the Intergovernmental Panel on Climate Change, edited by :

643 Stocker, T. F., Qin, D., Plattner, G.-K, Tignor, M., Allen, S. K., Boschung, J., Nauels,
644 A., Xia, Y., Bex, V., and Midgley, P. M., Cambridge University Press, Cambridge,
645 United Kingdom and New York, NY, USA, 2013.

646 Kanitz, T., Ansmann, A., Engelmann, R., and Althausen, D.: North-south cross
647 sections of the vertical aerosol distribution over the Atlantic Ocean from
648 multiwavelength Raman/polarization lidar during Polarstern cruises, *J. Geophys.*
649 *Res.*,118, 2643-2655, doi: 10.1002/jgrd.50273, 2013.

650 Kanitz, T., Engelmann, R., Heinold, B., Baars, H., Skupin, A., and Ansmann A.:
651 Tracking the Saharan Air Layer with shipborne lidar across the tropical Atlantic,
652 *Geophys. Res. Lett.*, 41, 1044-1050, doi: 10.1002/2013GL058780,
653 <http://dx.doi.org/10.1002/2013GL058780>, 2014.

654 Klett, J.D.: Stable analytical inversion solution for processing lidar returns, *Appl.*
655 *Optics*, 20, 211-220, doi: 10.1364/AO.20.000211, 1981.

656 Komppula, M., Mielonen, T., Arola, A., Korhonen, K., Lihavainen, H., Hyvärinen, A.
657 P., Baars, H., Engelmann, R., Althausen, D., Ansmann, A., Müller, D., Panwar, T. S.,
658 Hooda, R. K., Sharma, V. P., Kerminen, V. M., Lehtinen, K. E. J., and Viisanen, Y.:
659 Technical Note: One year of Raman-lidar measurements in Gual Pahari EUCAARI
660 site close to New Delhi in India - Seasonal characteristics of the aerosol vertical
661 structure, *Atmos. Chem. Phys.*, 12, 4513-4524, doi: 10.5194/acp-12-4513-2012, 2012.

662 Kulmala, M., et al., General overview: European Integrated project on Aerosol Cloud
663 Climate and Air Quality interactions (EUCAARI) – integrating aerosol research from
664 nano to global scales, *Atmos. Chem. Phys.*, 11, 13061-13143, doi: 10.5194/acp-11-
665 13061-2011, 2011.

666 Laakso, L., Vakkari, V., Virkkula, A., Laakso, H., Backman, J., Kulmala, M., Beukes,
667 J. P., van Zyl, P. G., Tiitta, P., Josipovic, M., Pienaar, J. J., Chiloane, K., Gilardoni,
668 S., Vignati, E., Wiedensohler, A., Tuch, T., Birmili, W., Piketh, S., Collett, K., Fourie,
669 G. D., Komppula, M., Lihavainen, H., de Leeuw, G., and Kerminen, V. M.: South
670 African EUCAARI measurements: seasonal variation of trace gases and aerosol
671 optical properties, *Atmos. Chem. Phys.*, 12, 1847-1864, doi: 10.5194/acp-12-1847-
672 2012, 2012.

673 Lourens, A. S. M., Butler, T. M., Beukes, J. P., van Zyl, P. G., Beirle, S., Wagner, T.
674 K., Heue, K. P., Pienaar, J. J., Fourie, G. D., and Lawrence, M. G.: Re-evaluating the
675 NO₂ hotspot over the South African Highveld, *S. Afr. J. Sci.*, 108, doi: 54-59,
676 10.4102/sajs.v108i11/12.1146, 2012.

677 Mamouri, R. E., Ansmann, A., Nisantzi, A., Kokkalis, P., Schwarz,
678 A. and Hadjimitsis D.: Low Arabian dust extinction-to-backscatter
679 ratio, *Geophys. Res. Lett.*, 40, 4762-4766, doi:10.1002/grl.50898, 2013.

680 Mamouri, R.E. and Ansmann, A.: Fine and coarse dust separation with polarization
681 lidar, *Atmos. Meas. Tech.*, 7, 3717-3735, doi:10.5194/amt-7-3717-2014, 2014.

682 Mishchenko, M., Travis, L.D., Kahn, R.A. and West, R.A.: Modeling phase functions
683 for dustlike tropospheric aerosols using a shape mixture of randomly oriented
684 polydisperse spheroids, *J. Geophys. Res.*, 102, 16831-16847, 1997.

685 Müller, D., Wandinger, U. and Ansmann, A.: Microphysical particle parameters from
686 extinction and backscatter lidar data by inversion with regularization: theory, *Appl.*
687 *Opt.* 38, 2346–2357, 1999a.

688 Müller, D., Wandinger, U. and Ansmann, A.: Microphysical particle parameters from
689 extinction and backscatter lidar data by inversion with regularization: simulation,
690 *Appl. Opt.* 38, 2358–2368, 1999b.

691 Müller, D., Wandinger, U., Althausen, D., and Fiebig, M.: Comprehensive particle
692 characterization from three-wavelength Raman-lidar observations, *Appl. Opt.*, 40,
693 4863–4869, doi:10.1364/AO.40.004863, 2001.

694 Müller, D., Mattis, I., Wandinger, U., Ansmann, A., Althausen, D., Dubovik, O.,
695 Eckhardt, S., Stohl, A.: Saharan dust over a central European EARLINET-AERONET
696 site: combined observations with Raman lidar and Sun photometer, *J. Geophys. Res.*,
697 108, doi:10.1029/2002JD002918, 4345, 2003.

698 Müller, D., Mattis, I., Wandinger, U., Ansmann, A., Althausen, D. and Stohl,
699 A.: Raman lidar observations of aged Siberian and Canadian forest fire smoke in the
700 free troposphere over Germany in 2003: Microphysical particle characterization, *J.*
701 *Geophys. Res.*, 110, D17201, doi:10.1029/2004JD005756, 2005.

702 Müller, D., Ansmann, A., Mattis, I., Tesche, M., Wandinger, U., Althausen, D., and
703 Pissani, G.: Aerosol-type dependent lidar ratios observed with Raman lidar, *J.*
704 *Geophys. Res.*, 12, D16202, doi:10.1029/2006JD008292, 2007.

705 Murayama, T., Okamoto, H., Kaneyasu, N., Kamataki, H., Miura, K., Application of
706 lidar depolarization measurement in the atmospheric boundary layer : Effects of dust
707 and sea-salt particles, *J. Geophys. Res.*, 104, 31781-31792, doi:
708 10.1029/1999JD900503, 1999.

709 Murayama, T., Masonis, S. J., Redemann, J., Aderson, T. L., Schmid, B., Living J. M.,
710 Russell, P. B., Huebert, B., Howell, S. G., McNaughton, C. S., Clarke, A., Abo, M.,
711 Shimizu, A., Sugimoto, N., Yabuki, M., Kuze, H., Fukagawa, S., Maxwell-Meier K.,
712 Weber, R. J., Orsini, D.A., Blomquist, B., Bandy, A., and Thornton, D.: An
713 intercomparison of lidar-derived aerosol optical properties with airborne
714 measurements near Tokyo during ACE-Asia, *J. Geophys. Res.*, 108, D23, 8651, doi:
715 10.1029/2002JD003259, 2003.

716 Murayama, T., Müller, D., Wada, K., Shimizu, A., Sekigushi, M., and Tsukamoto, T.:
717 Characterization of Asian dust and Siberian smoke with multi-wavelength Raman
718 lidar over Tokyo, Japan in spring 2003, *Geophys. Res. Lett.*, 31, L23103, doi:
719 10.1029/2004GL021105, 2004.

720 Nicolae, D., Nemuc, A., Müller, D., Talianu, C., Vasilescu, J., Belegante L., and
721 Kolgotin, A.: Characterization of fresh and aged biomass burning events using
722 multiwavelength Raman lidar and mass spectrometry, *J. Geophys. Res.*, 118, 2956-
723 2965, doi:10.1002/jgrd.50324, 2013.

724 Nisantzi, A., Mamouri, R.E., Ansmann, A., and Hadjimitsis, D.: Injection of mineral
725 dust into the free troposphere during fire events observed with polarization lidar at
726 Limassol, Cyprus, *Atmos. Chem. Phys.*, 14, 12155-12165, doi: 10.5194/acp-14-
727 12155-2014, 2014.

728 Noh, Y. M., Müller, D., Shin, D. H., Lee, H. L., Jung, J. S., Lee, K. H., Cribb, M., Li,
729 Z., and Kim Y. J.: Optical and microphysical properties of severe haze and smoke
730 aerosol measured by integrated remote sensing techniques in Gwangju, Korea, *Atmos.*
731 *Environ.*, 43, 879–888, doi:10.1016/j.atmosenv.2008.10.058, 2009.

732 Omar, A., Winker, D., Vaughan, M., Hu, Y., Trepte, C., Ferrare, R., Lee, K.,
733 Hostetler, C., Kittaka, C., Rogers, R., Kuehn, R., and Liu, Z.: The CALIPSO
734 Automated Aerosol Classification and Lidar Ratio Selection Algorithm. *J. Atmos.*
735 *Oceanic Technol.*, 26, doi: <http://dx.doi.org/10.1175/2009JTECHA1231.1> 1994–
736 2014, 2009.

737 Piketh, S. J., Swap, R. J., Maenhaut, W., Annegarn, H. J., and Formenti, P.: Chemical
738 evidence of long-range atmospheric transport over southern Africa, *J. Geophys. Res.*,
739 107, D24, 4817, doi: 10.1029/2002jd002056, 2002.

740 Piketh, S. J., Tyson, P. D., and Steffen, W.: Aeolian transport from southern Africa
741 and iron fertilization of marine biota in the South Indian Ocean, *S. Afr. J. Sci.*, 96,
742 244-246, 2000.

743 Pósfai, M., Simonics, R., Li, J., Hobbs, P. V., and Buseck, P. R.: Individual aerosol
744 particles from biomass burning in southern Africa: 1. Compositions and size
745 distributions of carbonaceous particles, *J. Geophys. Res.*, 108, 2156-2202, doi:
746 10.1029/2002JD002291, 2003.

747 Preißler, J., Bravo-Aranda, J. Wagner, F., Granados-MuñOZ, M. J., Navas-Guzmán,
748 F., Guerrero-Rascado, J.L., Lyamani, H., and Alados-Arboledas, L.: Optical
749 properties of free tropospheric aerosol from multi-wavelength Raman lidars over the
750 southern Iberian Peninsula, in: *Proceedings of the 9th International Symposium on*
751 *Tropospheric Profiling, l'Aquila, Italy (September 3-7, 2012)*, doi:ISBN 978-90-
752 815839-4-7, 2012.

753 Preißler, J., Wagner, F., Guerrero-Rascado, J.L., and Silva, A.M.: Two years of free-
754 tropospheric aerosol layers observed over Portugal by lidar, *J. Geophys. Res.*, 118,
755 3676-3686, doi:10.1002/jgrd.50350, 2013.

756 Queface, A. J., Piketh, S. J., Eck, T. F., Tsay, S. C., and Mavume, A. F.: Climatology
757 of aerosol optical properties in Southern Africa, *Atmos. Environ.*, 45, 2910-2921, doi:
758 10.1016/j.atmosenv.2011.01.056, 2011.

759 Radke, L.F., Heggs, D.A., Lyons, H., Brook, C.A., Hobbs, P.V., Weiss, R., and
760 Rasmussen, R.: Airborne measurements on smoke from biomass burning, in *Aerosols*

761 and Climate, edited by Hobbs, P.V. and McCormick, M. P., Deepak, A., Hampton,
762 VA, USA, 411–422, 1998.

763 Reid, J.S., Koppmann, R., Eck, T.F, and Eleuterio, D. P. : A review of biomass
764 burning emissions, part II. Intensive physical properties of biomass burning particles,
765 *Atmos. Chem. Phys.*, 5, 799-825, doi: 10.5194/acp-5-799-2005, 2005.

766 Reid, J. S., and P. V. Hobbs: Physical and optical properties of smoke from individual
767 biomass fires in Brazil, *J. Geophys. Res.*, 103, 32013–32031, doi:
768 10.1029/98JD00159, 1998.

769 Ross, K. E., Piketh, S. J., Bruintjes, R. T., Burger, R. P., Swap, R. J., and Annegarn,
770 H. J.: Spatial and seasonal variations in CCN distribution and the aerosol-CCN
771 relationship over southern Africa, *J. Geophys. Res.*, 108, D13, 8481, doi:
772 10.1029/2002JD002384, 2003.

773 Roy, D.P., Frost, P.G.H., Justice, C.O., Landmann, T., Le Roux, J.L., Gumbo, K.,
774 Makungwa, S., Dunham, K., du Toit, R., Mhwandagara, K., Zacarias, A., Tacheba,
775 B., Dube, O.P., Pereira, J.M.C., Mushove, P., Morisette, J.T., Santhana-Vannan S.K.,
776 and Davies, D.: The Southern Africa Fire Network (SAFnet) regional burned-area
777 product-validation protocol, *Int. J. Remote Sens.*, 26, 4265-4292, 2005

778 Roy, D. P., Boschetti, L., Justice, C. O. and Ju, J.: The collection 5 MODIS burned
779 area product – Global evaluation by comparison with the MODIS active fire product,
780 *Remote Sens. Environ.*, 112, 3960-3707, doi: 10.1016/j.rse.2008.05.013, 2008.

781 Schneider, P., Lahoz, W. A., and van der A, R.: Recent satellite-based trends of
782 tropospheric nitrogen dioxide over large urban agglomerations worldwide, *Atmos.*
783 *Chem. Phys.*, 15, 1205–1220, 2015.

784 Shimizu, A., Sugimoto, N., Matsui, I., Arao, K., Uno, I., Murayama, T., Kagawa, N.,
785 Aoki, K., Uchiyama, A., and Yamazaki, A.: Continuous observations of Asian dust
786 and other aerosols by polarization lidars in China and Japan during ACE-Asia, *J.*
787 *Geophys. Res.*, 109, D19S17, doi:10.1029/2002JD003253, 2004.

788 Shin, S.-K., Müller, D., Lee, C., Lee, K. H., Shin, D., Kim, Y. J. and Noh, Y. M.:
789 Vertical variation of optical properties of mixed Asian dust/pollution plumes

790 according to pathway of air mass transport over East Asia, *Atmos. Chem. Phys.*, 15,
791 6707-6720, doi:10.5194/acp-15-6707-2015, 2015.

792 Sugimoto, N., Uno, I., Nishikawa, M., Shimizu, A., Matsui, I., Dong, X., Chen, Y.,
793 and Quan, H.: Record heavy Asian dust in Beijing in 2002: Observations and model
794 analysis of recent events, *Geophys. Res. Lett.*, 30, 1640, doi:10.1029/2002GL016349,
795 2003.

796 Tesche, M., Ansmann, A., Müller, D., Althausen, D., Engelmann, R., Freudenthaler,
797 V., and Groß, S.: Vertically resolved separation of dust and smoke over Cape Verde
798 using multiwavelength Raman and polarization lidars during Saharan Mineral Dust
799 Experiment 2008, *J. Geophys. Res.*, 114, D13202, doi:10.1029/2009JD011862, 2009.

800 Tesche, M., Gross, S., Ansmann, A., Müller, D., Althausen, D., Freudenthaler, V., and
801 Esselborn, M.: Profiling of Saharan dust and biomass-burning smoke with
802 multiwavelength polarization Raman lidar at Cape Verde, *Tellus B*, 63, available at:
803 <http://www.tellusb.net/index.php/tellusb/article/view/16360> (last access: 14 December
804 2015), 2011.

805 Tesfaye, M., Sivakumar, V., Botai, J., and Tsidu, G. M.: Aerosol climatology over
806 South Africa based on 10 years of Multiangle Imaging Spectroradiometer (MISR)
807 data, *J. Geophys. Res.*, 116, D20216, doi: 10.1029/2011jd016023, 2011.

808 Tiitta, P., Vakkari, V., Croteau, P., Beukes, J. P., van Zyl, P. G., Josipovic, M.,
809 Venter, A. D., Jaars, K., Pienaar, J. J., Ng, N. L., Canagaratna, M. R., Jayne, J. T.,
810 Kerminen, V.-M., Kokkola, H., Kulmala, M., Laaksonen, A., Worsnop, D. R., and
811 Laakso, L.: Chemical composition, main sources and temporal variability of PM1
812 aerosols in southern African grassland, *Atmos. Chem. Phys.*, 14, 1909–1927, doi:
813 10.5194/acp-14-1909-2014, 2014.

814 Twomey, S.: *Introduction to the Mathematics of Inversion in Remotes Sensing and*
815 *Indirect Measurements*, Elsevier Scientific, New York, 1977.

816 Venter, A. D., Vakkari, V., Beukes, J. P., van Zyl, P. G., Laakso, H., Mabaso, D.,
817 Tiitta, P., Josipovic, M., Kulmala, M., Pienaar, J. J., and Laakso, L.: An air quality

818 assessment in the industrialised western Bushveld Igneous Complex, South Africa, S.
819 Afr. J. Sci., 108, 1059, doi: 10.4102/sajs.v108i9/10.1059, 2012.

820 Veselovskii, I., Kolgotin, A., Griaznov, V., Müller, D., Wandinger, U., and
821 Whiteman, D.N.: Inversion with regularization for the retrieval of tropospheric
822 aerosol parameters from multiwavelength lidar sounding, Appl. Opt. 41, 3685–3699,
823 2002.

824 Veselovskii, I., Kolgotin, A., Griaznov, V., Müller, D., Franke, K., and Whiteman, D.
825 N.: Inversion of multiwavelength Raman lidar data for retrieval of bimodal aerosol
826 size distribution, Appl. Opt., 43, 1180-1195, 2004.

827 Wandinger, U., and Ansmann, A.: Experimental determination of the lidar overlap
828 profile with Raman lidar, Appl. Opt., 41, 511-514, doi: 10.1364/AO.41.000511, 2002.

829 Wagner, F. and Silva, A. M.: Some considerations about Ångström exponent
830 distributions, Atmos. Chem. Phys., 8, 481-489, doi:10.5194/acp-8-481-2008, 2008.

831 Wandinger, U., Müller, D., Böckmann, C., Althausen, D., Matthias, V., Bösenberg,
832 J., Weiß, V., Fiebig, M., Wendisch, M., Stohl, A., Ansmann A., Optical and
833 microphysical characterization of biomassburning and industrial-pollution aerosols
834 from multiwavelength lidar and aircraft measurements, J. Geophys. Res., 107, 8125,
835 doi:10.1029/2000JD000202, 2002.

836 Weinzierl B., Sauer, D., Esselborn, M., Petzold, A., Veira, A., Rose, M., Mund, S.,
837 Wirth, M., Ansmann, A., Tesche, M., Gross, S., and Freudenthaler, V.: Microphysical
838 and optical properties of dust and tropical biomass burning aerosol layers in the Cape
839 Verde region – an overview of the airborne in situ and lidar measurements during
840 SAMUM-2, Tellus, 63B, 589-618, doi: 10.1111/j.1600-0889.2011.00566.x, 2011.

841 Wenig, M., Spichtinger, N., Stohl, A., Held, G., Beirle, S., Wagner, T., Jahne, B. and
842 Platt, U.: Intercontinental transport of nitrogen oxide pollution plumes, Atmos.
843 Chem. Phys., 3, 387-393, 2003.

844 Winkler, H., P. Formenti, D. J. Esterhuyse, R. J. Swap, G. Helas, H. J. Annegarn, and
845 Andreae, M.O. : Evidence for large-scale transport of biomass burning aerosols from

846 sunphotometry at a remote South African site: *Atmos. Environ.*, 42, 5569-5578, doi:
847 10.1016/j.atmosenv.2008.03.031, 2008.

848

849

850
851
852
853

TABLES

Table 1. Aerosol type, time and altitude range of aerosol layers used for optical and microphysical aerosol characterization

aerosol source	date	time [UTC]	height [m]	Extinction Coefficient [Mm ⁻¹]	
				355 nm	532 nm
urban / industrial	25 March 2010	18:00 – 19:50	2100 – 2670	196 ± 18	75 ± 12
	25 March 2010	18:00 – 19:50	2790 – 3450	190 ± 36	68 ± 14
	25 March 2010	18:00 – 19:50	1560 – 1980	260 ± 6	78 ± 12
	16 April 2010	21:20 – 23:54	1980 – 2250	147 ± 13	58 ± 9
	16 April 2010	21:20 – 23:54	2280 – 2520	129 ± 10	39 ± 4
	16 April 2010	21:20 – 23:54	2610 – 3180	196 ± 43	81 ± 14
	14 May 2010	18:00 – 00:00	930 – 1360	238 ± 37	127 ± 25
	15 May 2010	18:30 – 20:20	1380 – 1860	196 ± 26	86 ± 19
	15 May 2010	18:30 – 20:20	2250 – 2700	81 ± 7	28 ± 3
	30 November 2010	17:15 – 18:00	960 – 1300	121 ± 6	44 ± 13
	30 November 2010	17:15 – 18:00	1350 – 1920	146 ± 26	50 ± 11
	30 June 2010	17:00 – 18:00	1420 – 1620	101 ± 5	34 ± 5
	30 June 2010	17:00 – 18:00	1650 – 1830	71 ± 11	37 ± 7
	10 January 2011	19:15 – 20:15	1890 – 2160	303 ± 45	146 ± 31
	13 January 2011	21:00 – 22:00	1200 – 1800	342 ± 24	163 ± 17
	13 January 2011	21:00 – 22:00	1920 – 2250	267 ± 42	158 ± 29
13 January 2011	21:00 – 22:00	2430 – 2880	199 ± 23	68 ± 12	
biomass burning	1 October 2010	00:10 – 01:00	1090 – 1900	331 ± 9	158 ± 8
	5 October 2010	18:10 – 23:10	1115 – 1750	432 ± 62	227 ± 37
	5 October 2010	18:10 – 23:10	1980 – 2700	256 ± 18	132 ± 15
	6 October 2010	20:00 – 00:00	1175 – 1540	277 ± 27	142 ± 5
	6 October 2010	20:00 – 00:00	1565 – 2160	214 ± 14	111 ± 11
	6 October 2010	20:00 – 00:00	2190 – 2520	152 ± 6	85 ± 16
	6 October 2010	20:00 – 00:00	2610 – 2820	121 ± 19	80 ± 6
	21 October 2010	01:30 – 02:30	880 – 1530	261 ± 28	131 ± 20
	21 October 2010	01:30 – 02:30	1685 – 2280	168 ± 7	66 ± 16
	21 October 2010	01:30 – 02:30	2400 – 2880	171 ± 30	70 ± 14
	22 August 2010	00:00 – 01:00	1205 – 1565	340 ± 13	162 ± 8
	22 August 2010	00:00 – 01:00	1685 – 1920	354 ± 5	190 ± 8
22 August 2010	02:00 – 03:00	1115 – 1535	335 ± 6	163 ± 10	
22 August 2010	02:00 – 03:00	1745 – 2250	331 ± 15	170 ± 4	
mixed aerosols	16 August 2010	17:00 – 18:00	1115 – 1445	316 ± 24	151 ± 9
	16 August 2010	19:00 – 20:00	995 – 1265	296 ± 7	157 ± 11
	18 August 2010	19:00 – 20:00	1175 – 1355	154 ± 9	75 ± 4
	18 August 2010	19:00 – 20:00	1415 – 1715	174 ± 11	66 ± 4
	18 August 2010	19:00 – 20:00	1865 – 2160	184 ± 6	66 ± 3
	22 August 2010	17:00 – 18:00	1145 – 1505	286 ± 3	109 ± 4
	22 August 2010	17:00 – 18:00	1595 – 2040	267 ± 16	119 ± 8

854
855
856
857

858 **Table 2.** Mean value \pm standard deviation of aerosol lidar ratio at 355, particle depolarization ratio and
 859 Ångström exponent related to extinction between 355 and 532 nm for the examined aerosol types, as
 860 well as value of range and median
 861

aerosol source	mean \pm stdv	range	median
lidar ratio at 355 nm [sr]			
urban / industrial	52 \pm 7	41 – 59	54
biomass burning	92 \pm 10	81 – 119	88
mixed aerosols	74 \pm 11	59 – 90	73
lidar ratio at 532 nm [sr]			
urban / industrial	41 \pm 13	23 – 74	38
biomass burning	75 \pm 14	47 – 92	79
mixed aerosols	46 \pm 13	33 – 68	40
particle depolarization ratio at 355 nm [%]			
urban / industrial	0.9 \pm 0.4	0.3 – 1.7	1.0
biomass burning	3.2 \pm 1.3	1.2 – 5.7	2.7
mixed aerosols	8.3 \pm 0.7	7.3 – 9.1	8.1
ångström exponent related to extinction between 355 and 532 nm			
urban / industrial	2.3 \pm 0.5	1.3 – 3.0	2.4
biomass burning	1.7 \pm 0.3	1.0 – 2.4	1.7
mixed aerosols	2.0 \pm 0.4	1.6 – 2.5	2.0

862 **Table 3.** Mean value \pm standard deviation of effective radius and single-scattering albedo for the
 863 examined aerosol types, as well as range and median.
 864

Aerosol Source	mean \pm stdv	range	median
effective radius [μm]			
urban / industrial	0.10 \pm 0.03	0.07 – 0.16	0.09
biomass burning	0.17 \pm 0.04	0.11 – 0.28	0.17
mixed aerosols	0.13 \pm 0.03	0.09 – 0.19	0.13
single-scattering albedo at 532 nm			
urban / industrial	0.87 \pm 0.06	0.75 – 0.96	0.88
biomass burning	0.90 \pm 0.06	0.77 – 0.98	0.90
mixed aerosols	0.88 \pm 0.07	0.76 – 0.95	0.89
complex refractive index			
urban / industrial	1.61 (\pm 0.11) + 0.021 (\pm 0.010)i	1.47 – 1.78 (RRI) 0.007 – 0.039 (IRI)	1.64 (RRI) 0.020 (IRI)
biomass burning	1.43 (\pm 0.07) + 0.016 (\pm 0.011)i	1.35 – 1.57 (RRI) 0.002 – 0.046 (RRI)	1.40 (RRI) 0.015 (IRI)
mixed aerosols	1.52 (\pm 0.15) + 0.022 (\pm 0.015)i	1.33 – 1.74 (RRI) 0.004 – 0.046 (IRI)	1.56 (RRI) 0.019 (IRI)

865
 866

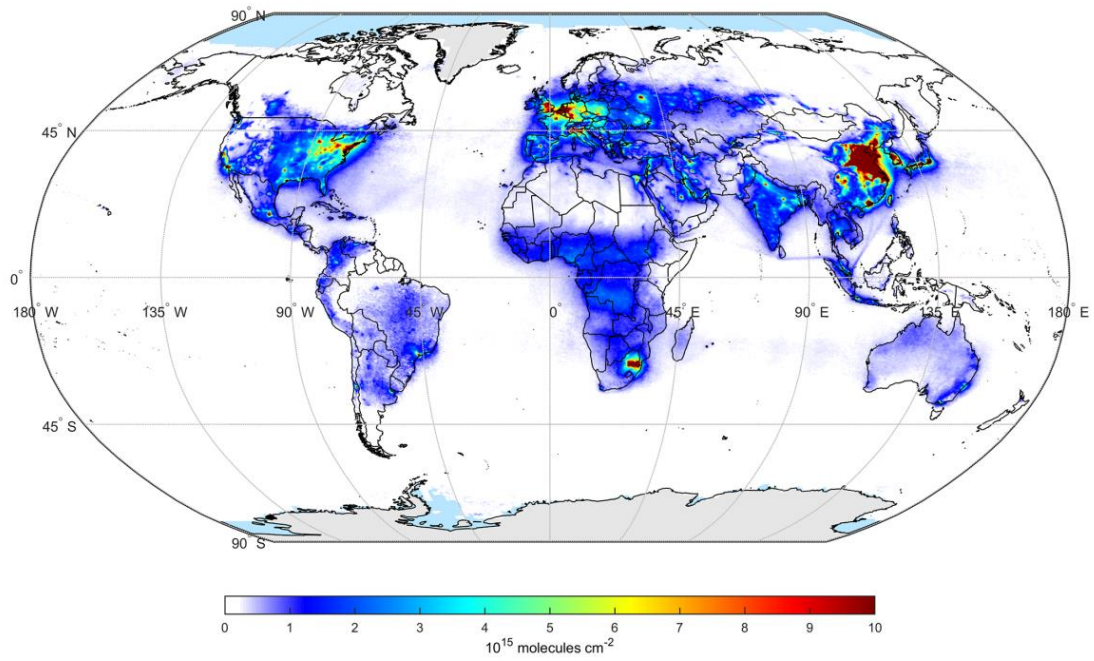
867 **Table 4.** The code used in Figure 7 and the respective reference.
868

Code	Reference
A03	Anderson et al., 2003
A05	Ansmann et al., 2005
A09a	Ansmann et al., 2009
A09b	Amiridis et al., 2009
A11	Arboledas et al., 2011
B03	Balis et al., 2003
B12a	Baars et al., 2012
B12b	Burton et al., 2012
B13	Burton et al., 2013
G10	Giannakaki et al., 2010
G11	Groß et al., 2011
G13	Groß et al., 2013
G16	This study
H15	Hesse et al., 2015
I15	Illingworth et al., 2015
K14	Kanitz et al., 2014
K12	Kompulla et al., 2012
M05	Müller et al., 2005
M07	Müller et al., 2007
M04	Murayama et al., 2004
M13	Murayama et al., 2013
N13	Nicolae et al., 2013
P12	Preißler et al., 2012
P13	Preißler et al., 2013
R98	Reid et al., 1998
T11	Tesche et al., 2011
W02	Wandinger et al., 2002
W11	Weinzierl et al., 2011
X08	Xie et al., 2008

869
870
871
872
873
874

875

FIGURES



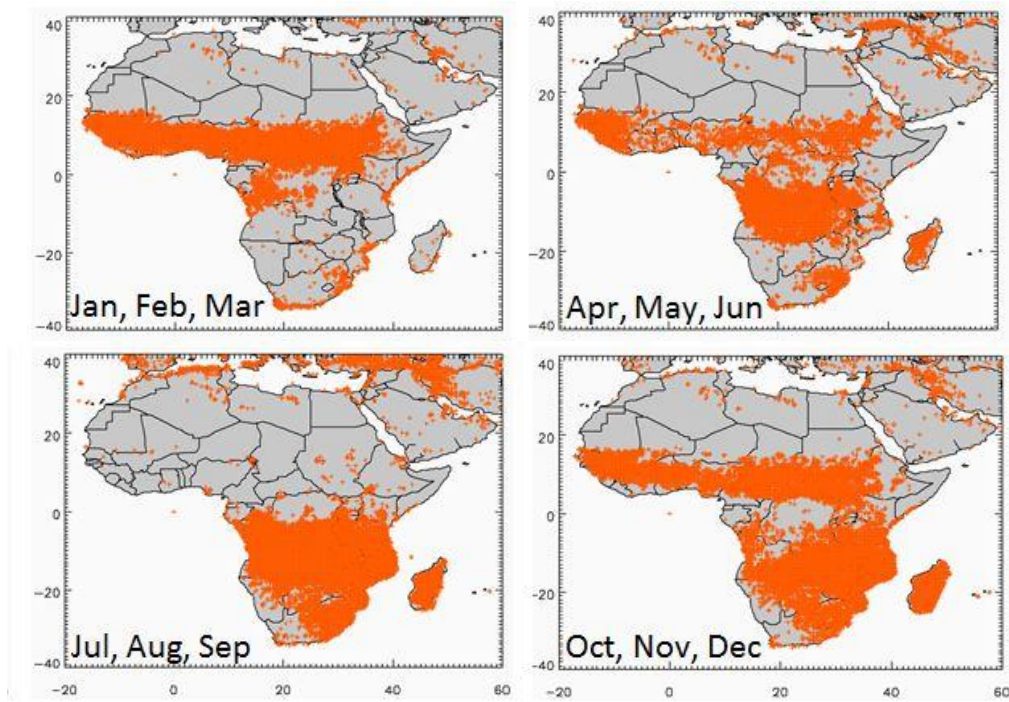
876

877

878

879 **Figure 1.** Global map of long-term average tropospheric NO₂ column derived from
880 SCIAMACHY data from August 2002 to March 2012 (Schneider et al., 2015)

881



902

903 **Figure 2.** Number of fire hotspots with confidence levels between 80-100% averaged
904 in terms of 3 months for the year 2010 in the latitude range between -40° and 40° and
905 longitude range between -20° and 60°

906
907
908
909
910
911
912
913
914
915
916
917
918
919
920
921
922
923
924
925
926

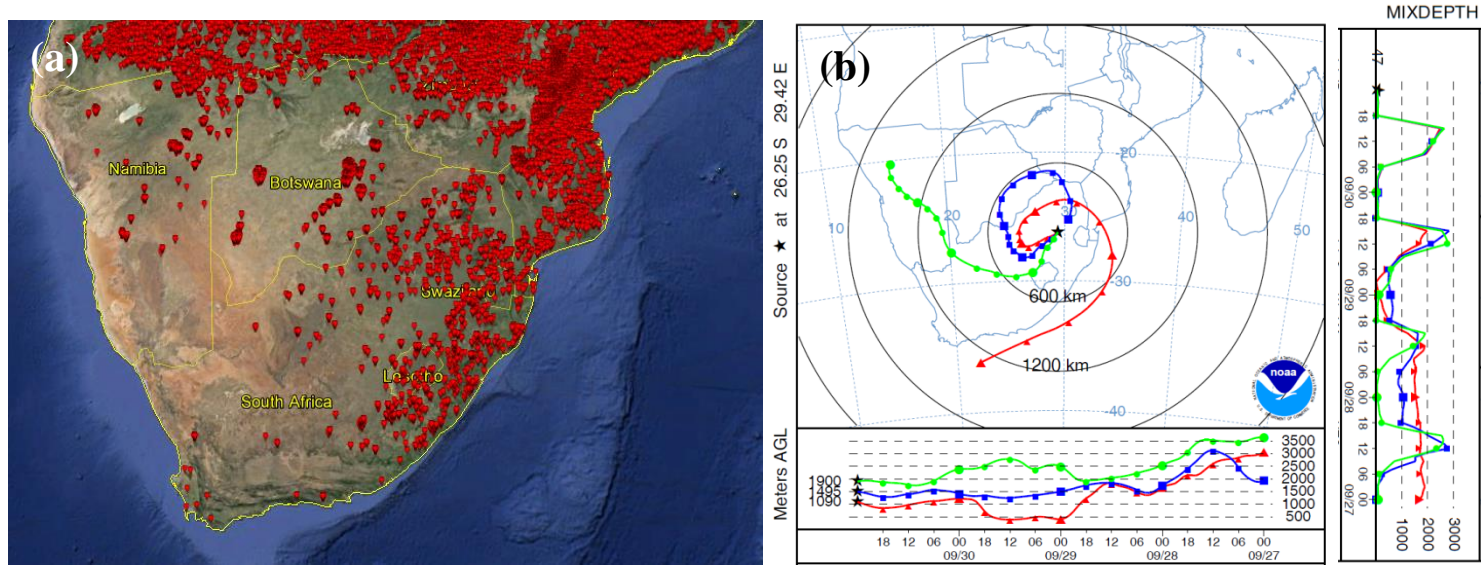
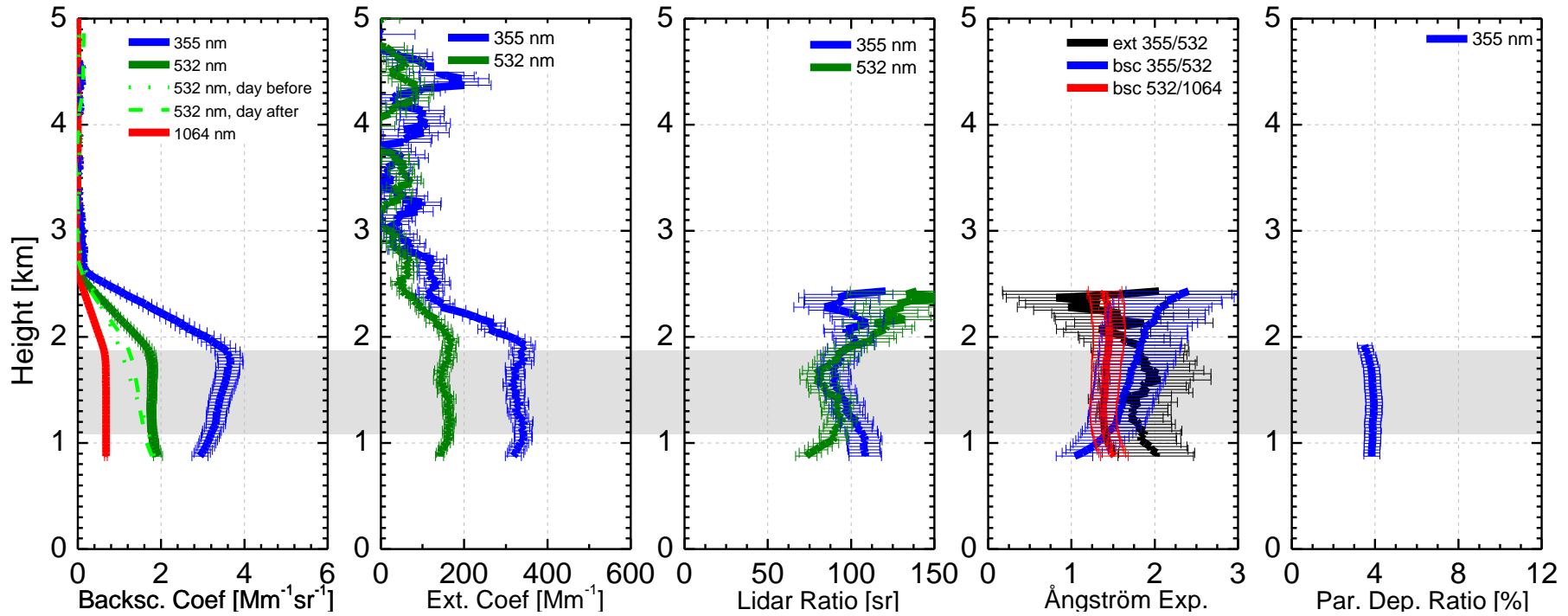


Figure 3. MODIS fire hotspots for the period 28 September 2010 – 01 October 2010 and for the latitude range between -35° and -15° W and the longitude range between 10° and 40° S (a). Four-day backward trajectories arriving at Elandsfontein on 1 October 2010 at 00:00 for arrival height of the bottom (1090 m), center (1495 m) and top (1900 m) of the aerosol layer observed (b).

927



928

929

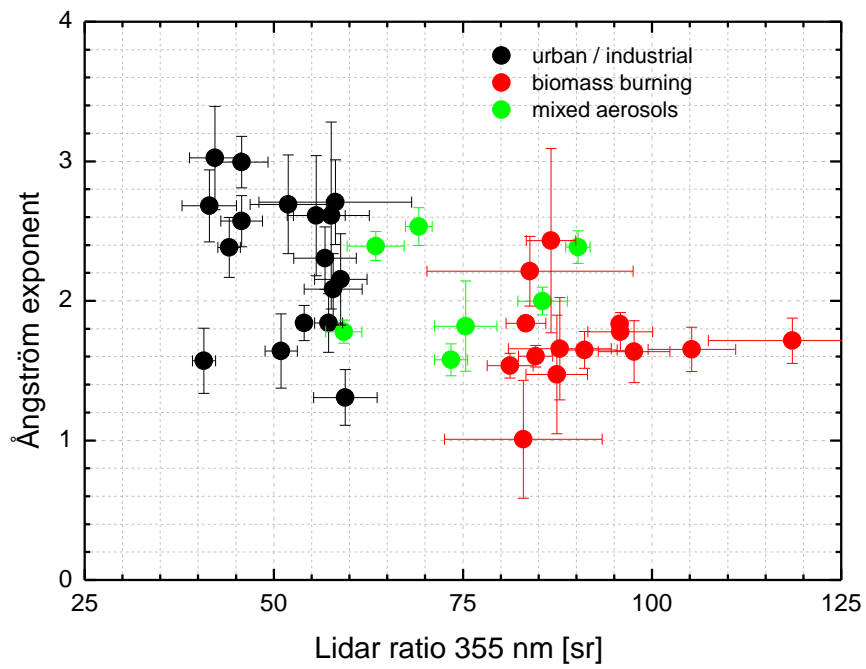
930

931

932

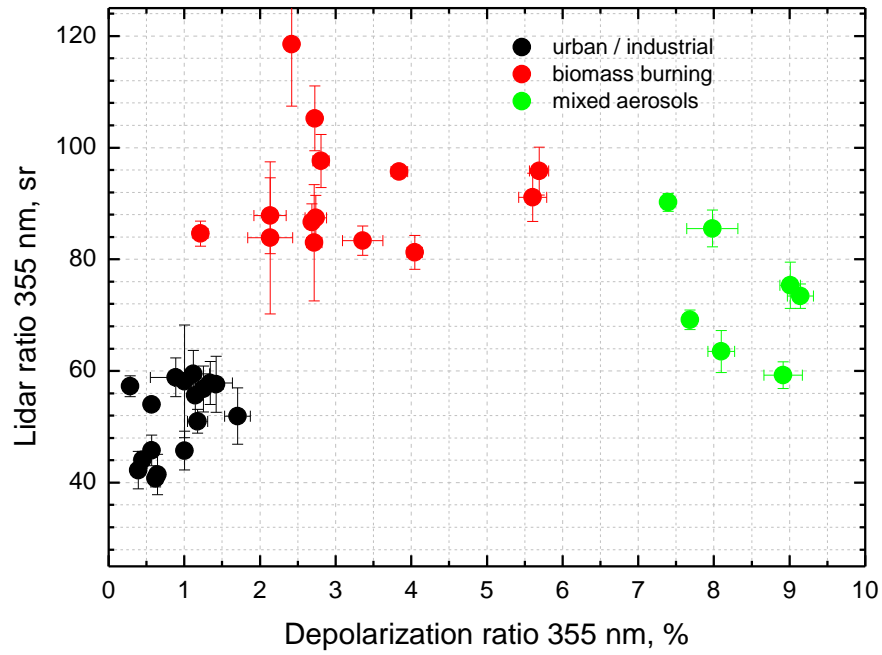
Figure 4. Backscatter coefficients, extinction coefficients, lidar ratios, Ångström exponents and particle depolarization ratio at Elandsfontein on 1 October 2010, 00:10 – 03:59 UTC

933
934
935



936
937
938
939

Figure 5. Lidar ratio at 355 nm versus the extinction-related Ångström exponent from 355 to 532 nm for the three aerosol types investigated in our study

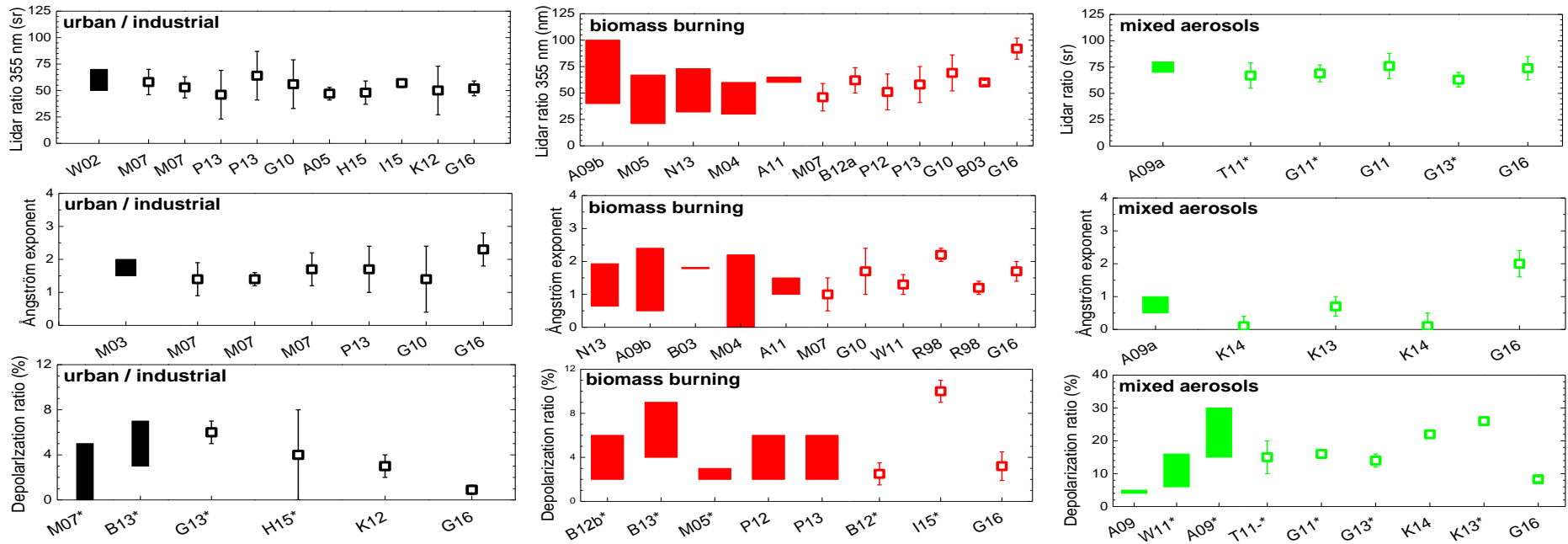


941

942

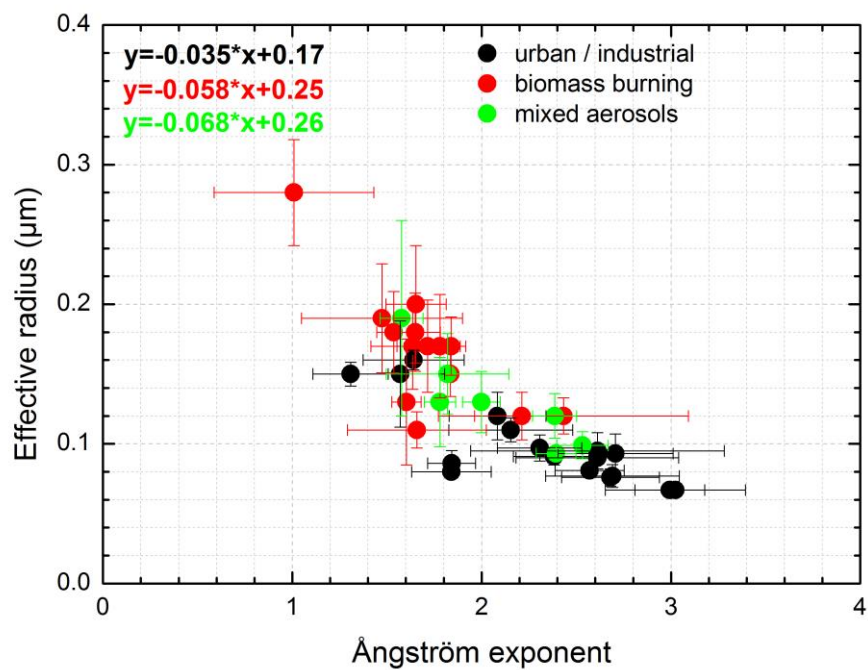
943

Figure 6. Lidar ratio at 355 nm versus the depolarization ratio at 355 nm for the three aerosol types investigated in our study



944
 945
 946
 947
 948
 949

Figure 7. General literature values for lidar ratio at 355 nm, Ångström exponent and depolarization ratio (355 or 532 nm) for urban/industrial (black), biomass burning (red) and for mixed biomass burning with desert dust aerosols (green). The x-axis are the studies presented in Table 4. Floating columns are referring to range values while the symbols are referring to mean values with one standard deviation. The depolarization values is at 355 nm except for the cases noted with asterisk (*) which are referring to visible wavelength (532 nm or 710 nm).



950
 951 **Figure 7.** Effective radius versus Ångström exponent for the three aerosol types
 952 investigated in our study.
 953